ChemCatChem

Research Article
doi.org/10.1002/cctc.202500978

Chemistry Europe
European Chemical Societies Publishing

www.chemcatchem.org

Elemental Analysis of Catalysts in a Fixed-Bed Reactor by Laser-Induced Breakdown Spectroscopy

Diego Espinoza,[a] Hemanth Appala,[a] Oliver Korup,[a] and Raimund Horn*[a]

In situ and operando characterization techniques provide molecular, surface, electronic, and structural information about catalysts in reactors. Accessing changes in the "Elemental Composition" of catalysts under reaction conditions remains yet an unsolved challenge. This work takes a first step in this direction by investigating the potential and limitations of Laser-Induced Breakdown Spectroscopy (LIBS) for monitoring catalyst deactivation, specifically during Dry Reforming of Methane over Ni/γ-Al_2O_3 and Propane Dehydrogenation over VO_X/γ-Al_2O_3. The study increases complexity stepwise, starting from spatially resolved ex situ LIBS analysis of catalyst particles removed from the reactor after reaction, to the development of a fiber-optic LIBS system and time-resolved intra-reactor measurements. Spectroscopic measurements are complemented by monitoring catalyst activity and temperature at each stage. For the dry reforming of methane, a correlation was found between catalyst performance, temperature, and the spatial distribution of coke, with distinct zoning along the catalyst bed. A cost-effective fiber-optic LIBS probe was developed, allowing for intra-reactor measurements under harsh conditions. The LIBS probe was used to study catalyst deactivation and regeneration during propane dehydrogenation by measuring time-resolved carbon and vanadium profiles. A Partial Least Squares regression model was developed to correlate the amount of carbon deposits with the LIBS spectra, allowing the derivation of quantitative statements. Despite its limitations, such as invasiveness and gas sensitivity, the study highlights the potential of LIBS as an in situ/*operando* elemental analysis technique.

1. Introduction

Climate change, the finite nature of fossil resources and the ever-increasing global energy demand require strong research efforts to produce chemicals more sustainably. Heterogeneous catalysis plays a crucial role in this endeavor; it is estimated that approximately 90% of chemical production is assisted by a solid catalyst[1] These extremely complex materials show a highly dynamic behavior, meaning that changes in temperature, pressure, or composition of the reaction mixture inside of the reactor lead to changes in the surface/bulk structure, type of active sites, and changes in the electronic properties of the material. Any information on how this happens inside of catalytic reactors will aid in the proposition of congruent reaction mechanisms and structure-activity relationships and will ultimately contribute to the design of more sustainable and energy-efficient processes.[2]

One opportunity to gain this understanding is through the application of in situ and *operando* spectroscopy. These techniques provide molecular, surface, electronic, and structural information about a catalyst under reaction conditions. However, one piece of information that is hardly accessible yet is the change in the "Elemental Composition" of a catalyst material under reaction conditions.[3–5] This is a severe deficit, considering that catalyst deactivation by coking, poisoning, or catalyst moderation by promoters or inhibitors is frequently encountered in industrial catalysis.

In situ/*operando* spectroscopic measurements require often a compromise between analysis under ideal laboratory conditions and analysis under harsh industrial reaction conditions. Traditional elemental analysis methods, such as electrothermal atomization-atomic absorption spectroscopy (ETA-AAS), Inductively coupled plasma-atomic emission spectroscopy (ICP-AES), and inductively coupled plasma-mass spectroscopy (ICP-MS), cannot be used for the remote analysis of heterogeneous catalysts in reactors, because all of these methods would require to take a sample from the catalyst inventory.[6]

On the other hand, synchrotron-based methods such as X-Ray absorption spectroscopy (XAS) and X-Ray fluorescence (XRF) are only partially applicable. First, they require synchrotron-based facilities, only available in some parts of the world, sophisticated instrumentation, high capital costs, precise experimental planning, and limited beam time access. This means that long-term catalyst deactivation can usually not be studied.[7,8] Second, suitable sample environments that offer optical access are required.[9,10]

In this context, a comparably recent laser spectroscopy technique, laser-induced breakdown spectroscopy (LIBS), can bridge between these two perspectives, offering the possibility to perform remote analysis at hardly accessible locations with high spatial and temporal resolution and multielement detection

[a] D. Espinoza, H. Appala, Dr. O. Korup, Prof. Dr. R. Horn
Institute of Chemical Reaction Engineering, Hamburg University of Technology, Hamburg 21073, Germany
E-mail: horn@tuhh.de

Supporting information for this article is available on the WWW under https://doi.org/10.1002/cctc.202500978

capabilities. In comparison to the above-mentioned techniques, a LIBS setup is rather simple and inexpensive.[11–13]

LIBS is an analytical method that relies on the principle of atomic emission spectroscopy. A high-energy laser pulse is used to vaporize a small amount of the sample where the laser pulse hits, converting it to the plasma state. When the plasma cools, it subsequently decays, emitting element-specific radiation. This radiation is recorded as a function of wavelength using a spectrometer. While the position of the lines and bands allow a qualitative detection of atoms and molecular fragments in the plasma plume and thus the sample, the intensities of the lines contain quantitative information about the elemental contents of the sample.[14]

Due to its versatility, LIBS applications have been reported in fields such as medical sciences, geomaterials, explosives, recycling, space exploration, forensics, and agriculture.[15] In heterogeneous catalysis, the applications of LIBS have been limited to the ex situ analysis of solid catalysts, with focus on elemental imaging and optical setup optimization.

For example, Laserna et al. reported the first contribution of LIBS in this field in the early 2000s. During this work, the suitability of LIBS for the determination of vanadium (V) in pellets of TiO_2-SiO_2 supports was evaluated.[16] Other investigations of the same research group demonstrated the applicability of LIBS for the generation of 2D multi-elemental maps of active material (Pt, Pd) and poisoning agents (P, Zn, Pb) in gasoline and diesel automobile catalytic converters.[17,18] Motto–Ross et al. showed the capability of LIBS to perform quantitative imaging measurements using a palladium-based (Pd) porous alumina catalyst as a model system.[19] A subsequent study evaluated the diffusion of trace metals (V, Ni, S) on supported alumina catalysts using 2D elemental maps. This process is particularly relevant in heavy oil upgrading, such as in the hydrodemetallization of oil residues. The experimental LIBS profiles improved the understanding of metal removal efficiency in the catalyst support by comparing it with simple transport models.[20]

In this work, we explore the potential and limitations of LIBS as an in situ/*operando* reactor diagnostic technique. As a model system, we investigated dry reforming of methane (DRM) on a supported Ni/γ-Al_2O_3 catalyst and propane dehydrogenation (PDH) on a supported VO_X/γ-Al_2O_3 catalyst. Active metal distributions (Ni, V) and poisons (C) were recorded in combination with activity and temperature profiles. Complexity was increased stepwise, starting from spatially resolved ex situ characterization of aged catalysts extracted from the reactor, followed by the development of a remote fiber optic LIBS system (FO-LIBS) and, finally, time-resolved in situ measurements.

2. Results and Discussion

2.1. Methane Dry Reforming (DRM)

As a first test system, the catalytic dry reforming of methane (DRM) on a supported Ni/γ-Al_2O_3 catalyst was studied in a spatially resolved manner (Equation (1)). The feed mixture was composed of CH_4 and CO_2 reacting to produce CO and H_2.

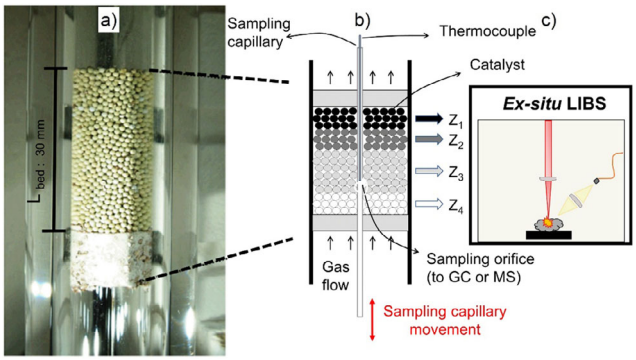

Figure 1. a) Schematic of semi-pilot profile reactor employed in methane dry reforming. b) Working principle of spatial profiling technique for simultaneous concentration and temperature measurements. c) Layer-by-layer ex situ LIBS characterization.

This reaction can have a positive environmental impact, since it can convert two strong greenhouse gases CH_4 and CO_2 to synthesis gas for the production of renewable fuels. Transition metals, especially nickel, are often used as catalysts, showing good activity and selectivity at moderate costs. The drawback of transition metal catalysts is their tendency to deactivate with time-on-stream by coking, limiting long-term applications.[21–24]

$$CH_4 + CO_2 \leftrightarrow 2CO + 2H_2 \quad H^0_{298K} = 247,3 kJ/mol \tag{1}$$

LIBS was used to spatially resolve elemental gradients caused by deactivation in an ex situ manner. Intra-reactor species and temperature profiles were recorded to complement the ex situ LIBS data. Further details are provided in the experimental section.

2.2. Spatially Resolved Experiments

To evaluate the changes in the elemental composition of the catalyst as a result of coking, molecular emissions in the CN violet band ($\Delta v = 0$) and the C_2 band ($\Delta v = 0$) of carbon were employed. Pretests under atmospheric conditions, using pure carbon standards, showed intense molecular emission bands in the 350–570 nm range. Weaker emissions of the main atomic carbon lines in the ultraviolet region, namely C (I) at 193,1 nm and C (I) at 247,8 nm, have also been detected. Molecular emission lines are, therefore, more sensitive for carbon detection than atomic lines, in agreement with several reports in the LIBS community focusing on carbon analysis.[25–27]

As illustrated in Figure 1, capillary sampling was used to record spatially resolved species and temperature profiles in the reactor. In this method, a thin sampling capillary slides through the center of the catalytic bed. The capillary has a small side sampling orifice for continuous sampling of a small fraction of the reaction mixture into an analytical instrument, here a mass spectrometer. The local temperature within the bed was measured by means of a thermocouple, tip-aligned with the orifice. By moving the capillary relative to the catalyst bed, gas species and temperature profiles could be measured. Changes in the reaction

mixture composition were evaluated by monitoring the mass-to-charge ratios: H_2 (2 amu), CH_4 (15 amu), CO (28 amu), Ar (40 amu), and CO_2 (44 amu). Argon was used as internal standard. Signal contributions to peak 28 amu were corrected by subtracting the contribution from CO_2. Water was calculated from the atom species balance of the reaction mixture. To validate this approach, the total mass balance was evaluated, closing better than 3,5%, which is a good value for species quantification by mass spectrometry.

This set of experiments provided three important pieces of information from inside the catalyst bed: i) species concentration, profiles, ii) temperature profiles, and iii) LIBS profiles. Figure 2 summarizes the results.

Interpreting the measured species, temperature and LIBS profiles is not straightforward, as they are the result of a number of interconnected chemical, physical, and mathematical effects. Two features of the profiles are eye-catching. While there is coking of the Ni-catalyst along the entire catalyst bed as revealed by LIBS (Figure 2c), the catalytic performance is very stable and both sets of profiles are very similar even though they were measured 4 h apart (Figure 2a,b,e–f). One way to explain this behavior could be, that on this nickel catalyst, nondeactivating carbon is formed, e.g. in form of filaments carrying the Ni-nanoparticles at their tip, maintaining catalytic activity.[28,29] This interpretation is supported by the detection of nickel signals along the bed by LIBS, irrespective of the coke loading (Figure 2d).

Second, there are distinguishable zones inside the catalyst bed. In the first zone, Z_1, stretching from the beginning of the catalyst bed at 0 mm to about 4 mm into the bed, methane dry reforming dominates, following approximately a stoichiometry $CH_4 + CO_2 \rightarrow 2CO + 2H_2$. CH_4 and CO_2 are converted at almost equal rates and CO and H_2 are formed at almost equal rates. However, due to the high diffusivity of H_2, H_2 diffuses against the flow direction and H_2 is detected already several millimeters upstream of the catalyst bed. This leads to a smearing out of the H_2 profile, and a less sharp onset compared to the heavier molecules CH_4, CO, and CO_2. Because H_2O could not be measured and had to be calculated from the H-balances, the apparent H_2O formation in zone 1 is at least in parts due to the "missing" hydrogen. Before the catalyst bed begins, the temperature profile rises fast from about 430 °C–540 °C due to heat transfer from the furnace surrounding the reactor tube which was set to 720 °C. Once the reaction mixture hits the catalyst bed, the temperature rise slows down, because part of the heat flowing in the catalyst bed is consumed by the endothermic dry reforming. The slope of the temperature profile becomes zero at around 4 mm, marking the end of zone Z_1 and the beginning of zone Z_2 in which the slope of the temperature profile becomes negative. In zone Z_2, stretching from about 4 mm to about 10 mm, the temperature decreases due to endothermic chemistry. While the rate of Equation (1) remains almost unchanged as can be seen from the unchanged slope of the CH_4 profile, a second and more rapid endothermic reaction kicks in, the reverse water gas shift (RWGS) reaction (Equation (2)).

$$CO_2 + H_2 \leftrightarrow CO + H_2O \quad H^0_{298K} = 41,3 kJ/mol \tag{2}$$

This is most clearly visible from the profiles of CO, H_2 and CO_2. While CO formation and CO_2 consumption increase noticeably at 4 mm, the slope of the H_2 formation remains almost constant. This seems at first glance counterintuitive as RWGS consumes H_2 and a drop-in slope of the H_2 profile would be expected. The slope of the H_2 profile does not change noticeably because enhanced back diffusion of H_2 compensates for H_2 conversion by RWGS.

At 10 mm into the catalyst bed, the slope of the temperature profile changes sign again, marking the end of zone Z_2 and the beginning of zone Z_3. At the beginning of zone Z_3, the H_2O profile levels off while CO and H_2 increase parallel to each other until about 25 mm. In line with the parallel decrease of CH_4 and CO_2 and increase of CO and H_2, respectively, this means stoichiometrically that DRM (Equation (1)) prevails in Z_3 while RWGS (Equation (2)) is basically ineffective. The slight increase of H_2O in zone Z_3 is a physical/mathematical artifact because the missing H_2 due to back diffusion is mathematically compensated by H_2O which is computed from the H-atom balance. Because the rate of DRM is comparatively low, heat flow into the catalyst bed overcompensates the endothermic heat consumption and the temperature rises monotonically up to about 25 mm.

The end of zone Z_3 at about 25 mm into the catalyst bed is marked by a deviating slope of the CO and H_2 profiles. At this point zone Z_4 begins, stretching until the end of the catalyst bed at 30 mm. Approaching the end of the catalyst bed, both, the CO and the H_2 profiles level off. However, due to the higher back diffusion of H_2, the H_2 profile levels off earlier. While CH_4 and CO_2 were measured by mass spectrometry and decrease monotonously and in parallel until the end of the catalyst bed, H_2O, which was calculated from the H-atom balance seems to increase from 25 mm on, which is however not a true water formation rather than a mere mathematical compensation for the missing H_2 due to back diffusion.

All along the catalyst bed, but in particular between the bed inlet at 0 mm and about 25 mm (Zones 1–Zone 3), strong CN-signals are detected by ex situ LIBS indicating coking (Figure 2c). Small but measurable Ni-signals are detected in Zone 1–Zone 3 as well (Figure 2d). Scanning electron micrographs (SEM) of catalyst spheres extracted from these zones (Figure 3a,b) show that the originally smooth γ-Al_2O_3 spheres are covered with a scaly shell of porous carbonaceous deposits in which the catalytically active Ni-sites remain obviously accessible to the reactants. At the beginning of Zone 4, approximately 25 mm into the bed, the normalized band areas of CN start decreasing, indicating coke removal. In line with this, the LIBS signals of Ni start increasing steeply. Figure 3d shows the corresponding LIBS spectra. Catalyst spheres extracted from Zone 4 and investigated by SEM do not show macroscopic amounts of coke (Figure 3c). The spheres look smooth, almost "like as prepared". Elemental distributions of carbon and nickel were confirmed by performing energy dispersive spectroscopy (SEM-EDS) of the aged samples, the results are presented in the Figure S1.

As carbon deposition is thermodynamically favored at low temperatures and high methane concentrations,[22] it is understandable that coke deposition decreases toward the end of the catalyst bed where temperatures above 600 °C are reached

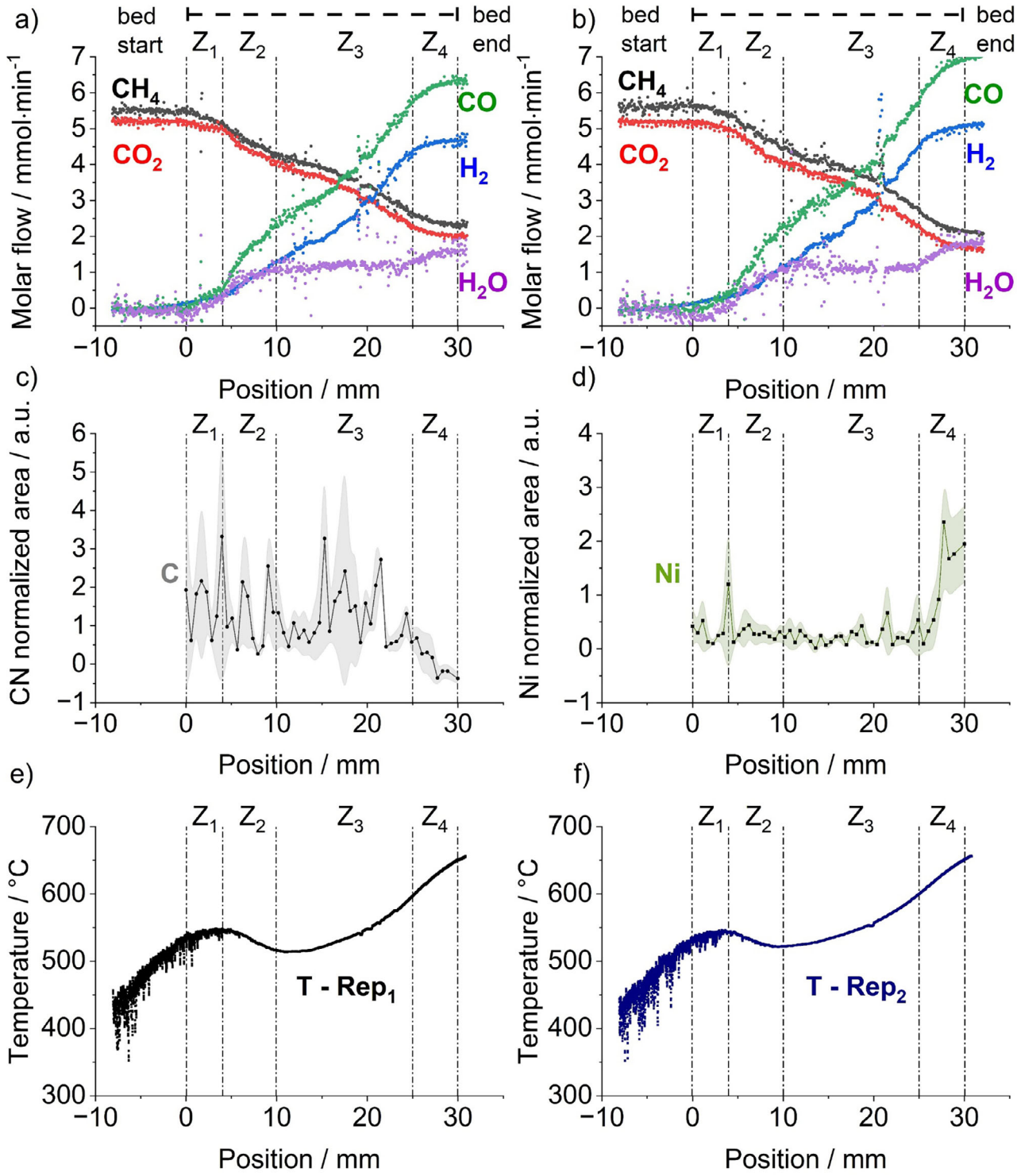

Figure 2. Reactor profiles measured for dry reforming of methane. a), b) Species profile replicates. c), d) Carbon and nickel ex situ elemental profiles and standard deviation. e), f) Temperature profile replicates. Reaction conditions: Feed composition $CH_4/CO_2/Ar$ = 25/25/50, 500 mL min^{-1}, 720 °C, 1 bar, 30 mm catalyst bed, 20 wt.% Ni//γ-Al_2O_3. LIBS conditions: 1-shoot, 3 replicates, 1.8 µs acquisition delay, 50 mJ/pulse, CN band ($\Delta v = 0$) at 388,3 nm, and Ni (I) at 341,4 nm.

and the methane concentration is low. A similar tendency was reported in a recent study from Colombo et.al.,[30] where spatially resolved operando Raman studies were performed to resolve carbonaceous deposits over a Rh/α-Al_2O_3 catalyst in an annular reactor. The authors provided mechanistic insights, emphasizing that carbon deposition is significantly influenced by methane concentration and the CO_2/CH_4 ratio.

In addition to validation, the SEM images provide an impression of the invasiveness and surface sensitivity of the method. The catalyst sphere shown in the SEM picture in Figure 3b was

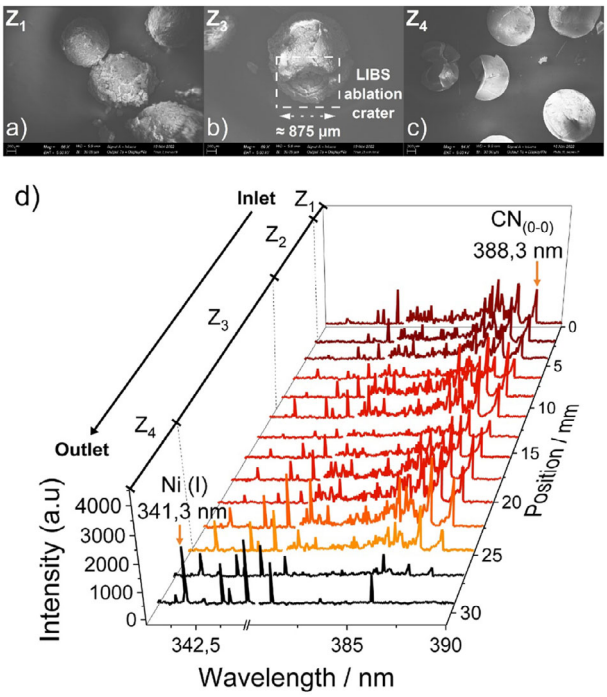

Figure 3. Scanning electron micrographs of spent catalyst particles from: a) entrance (Z1), b) middle (Z3), and c) outlet (Z4) reactor zone. d) Spatially resolved detection of nickel and carbonaceous deposits after reaction. Reaction conditions: Feed composition CH4/CO2/Ar = 25/25/50, 500 mL min^{-1}, 720 °C, 1 bar, 30 mm catalyst bed, 20 wt% Ni//γ-Al_2O_3. LIBS conditions: 1-shoot, 3 replicates, 1.8 µs acquisition delay, 50 mJ /pulse, CN band ($\Delta v = 0$) at 388,3 nm, and Ni (I) at 341,3 nm.

exposed to a LIBS pulse. According to literature the average ablation rate (AAR) for LIBS ranges between 1 and 5 µm/pulse.[31] However, this property is strongly material dependent, for this study a worst-case scenario with an ablation rate of 30 µm/pulse was estimated. By analyzing the magnitude of the estimated ablation rate, we can clearly state that from the perspective of heterogenous catalysis, LIBS is a bulk analysis method. True surface-sensitive techniques should probe the top atomic layers (nm range), like X-ray photoelectron spectroscopy (XPS) or auger electron spectroscopy (AES).

Whether the ablation rate, or invasiveness of LIBS is a problem or not will depend on the application and the question to be answered. For resolving elemental gradients along an industrial reactor containing between kilograms to tons of catalyst, LIBS ablation will be negligible, and the bulk character of the method will be of advantage. In laboratory reactors filled with milligrams of catalyst, sample ablation might be problematic, potentially biasing the sample composition by depth profiling, as well as inducing surface changes (e.g., oxide formation), due to high local temperature from the micro-plasma. The destructive nature of the laser ablation does not allow for the averaging of several measurements at the same sample position. It is desirable to sample always a fresh position and to limit analysis to a one-shot sampling scheme. Also, if surface-specific elemental information is required or if sub-millimeter elemental gradients must be resolved, LIBS is not the proper method. The most promising systems to apply LIBS to are possibly those in which a fresh catalyst is continuously moving through the detection volume, e.g., stirred tanks with solid catalyst in slurry phase or transport reactors with fluidized catalyst particles.

Overall, it was possible to find a correlation between the changes in catalytic activity, temperature, and catalyst elemental distribution along the reactor bed. LIBS was able to provide multi-element information in a time efficient manner. The elemental distributions of carbon and nickel were in good agreement with SEM/EDS observations. However, it is important to highlight that at this point we cannot strictly speak from a structure-activity relationship since the LIBS analysis was performed in an ex situ manner. Nevertheless, these first experiments can serve as benchmark and proof of concept.

2.3. Fiber-Optic LIBS Development (FO-LIBS)

A major challenge in conducting spectroscopic diagnostics in industrial reactors is achieving optical access. These reactors are usually made from stainless steel and operate under harsh conditions, including high temperatures, high pressures, and dangerous reaction mixtures. Optical fibers offer a practical solution to this problem, as they are made from fused silica, a chemically inert material capable of withstanding high temperatures. This property allows placing of a fiber optic probe directly into a harsh reaction environment. The second stage of this work focused on developing a fiber-optic LIBS setup (FO-LIBS) that allows intra-reactor analysis of catalysts inside fixed-bed reactors. Since this type of configuration is not commercially available, mainly due to the challenge of high energy fiber-laser coupling, a custom solution was developed. The design process was approached with a focus on simplicity, cost-effectiveness, and robustness. We tackled it by breaking the process into two essential tasks, delivery, and decoupling. Efforts were made to optimize each one of the tasks. In this section, the key capabilities of the optical setup are discussed, and further operational details are included in the experimental section.

When coupling a high-energy pulsed laser into an optical fiber, several challenges need to be addressed, such as surface breakdown at the fiber entrance face, air breakdown in the focal region, refocusing on the fiber entry segment, and fiber outer face damage.[32] To address these challenges the following strategy was employed. First, the coupling irradiance was ensured to be below the damage threshold of the fiber. This was achieved by using a large core multimode fiber (0.39 NA, 1500 µm core, Thorlabs FT1500 UMT) and tuning the laser pulse energy to a safe level. Second, the fiber inlet and outlet face were prepared by cleaving, providing a fault-free surface and decreasing the breakdown probability when coupling. Third, a micro-lens array (MLA) was employed to homogenize the beam profile to a top-hat distribution, avoiding the typical high-intensity region of Gaussian beams. Overall, this optical configuration offers the advantage of minimizing irradiance at the fiber entrance, reducing the risk of face or air breakdown. Additionally, it circumvents the use of vacuum chambers at the coupling site, which are typically

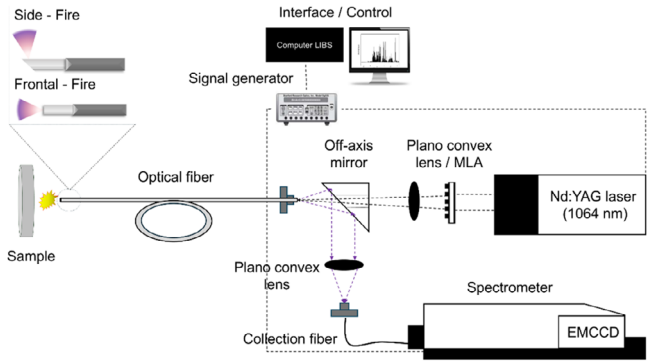

Figure 4. Schematic representation of the in situ LIBS optical setup. The upper left magnification shows the frontal / side-fire configuration of the fiber-optic LIBS probe.

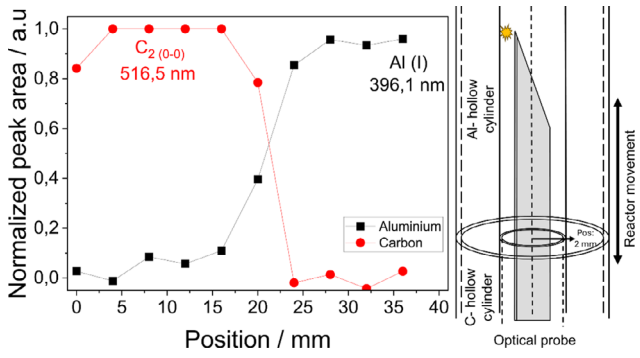

Figure 5. Determination of the spatial resolution for the in situ LIBS experimental setup. The right-side image exemplifies the side-fire sampling configuration between two hollow cylinders of graphite and aluminum.

associated with difficulties in alignment and fiber exchange.[33,34] LIBS is typically conducted with high-energy pulsed lasers, often emitting at an invisible wavelength of 1064 nm. Therefore, it is essential to adhere to all Class 4 laser safety regulations.

Figure 4 shows a general overview of the optical setup. In this configuration the optical fiber probe is responsible for delivering the excitation pulse to the sample and simultaneously collecting the plasma LIBS signal. This single-fiber configuration offers the advantage of automatic alignment for plasma signal collection, as the excitation pulse and the plasma are located along the same symmetry axis. Pulse energies (E_p) in the range of 90–100 mJ were coupled into the fiber, the spot size at the coupling site was adjusted to cover around 85% of the core of the optical fiber, reducing the irradiance at this position. The expected irradiance at the entrance of the fiber was on the order of $I_{in} \approx 1{,}5$ GW cm^{-2}, a value that is below the practical breakdown threshold reported by the fiber manufacturer (1-5 GW cm^{-2}). We found the coupling efficiency to be around 55%, aligning with reported values for multimode fibers.[35–37] On the delivery side, the fiber-sample distance ranged from 1 to 2 mm. At this point, the expected irradiance level reached about 0,5 GW cm^{-2}, surpassing the threshold for plasma formation on solid materials, reported to be in the order of 0,01 GW cm^{-2}.[38] Fiber lifetime was assessed by successfully shooting over 100 pulses without any signs of fiber damage.

The selection of signal decoupling optics had a direct impact on the amount of information that we could gain from the plasma formation process. Therefore, the right choice of the optical element was essential at this stage. Typical options include the use of dichroic mirrors (DM) and hole-centered mirrors. In this design the use of an off-axis parabolic mirror (OAP) was preferred for two main reasons. The first one is because it allows the decomposition of the signal without interposing wavelength sensitivity, as in the case of dichroic mirrors (DM). This allows to use the system in different spectral regions (UV and VIS), simplifying the simultaneous analysis of sample elements. Second, the hole located in the OAP allows the coupling of the excitation pulse in the fiber without adding extra losses and, more importantly, without introducing a damage threshold constraint, which would need to be considered in the case of DM.[39–41]

2.4. Sampling Mode

The fiber-optic LIBS system (FO-LIBS) can be employed in two configurations to perform frontal as well as side firing, as indicated by the magnified view in Figure 4. Each configuration brings advantages and disadvantages. In the case of frontal sampling, better plasma formation and, therefore, a stronger LIBS signal is obtained. However, this mode would not allow performing spatially resolved measurements in a profile because catalyst and optical fiber would be in coaxial arrangement. The side-fire configuration allows probing in a 90° angle to the fiber axis and therefore even spatial measurements along the reactor axis, but at the cost of lower collection efficiency and lower damage threshold at the distal tip of the fiber.

To demonstrate this advantage, a straightforward experiment was performed to determine the spatial resolution that can be reached with a side-fire fiber. An artificial step gradient in elemental composition along the axial direction was created using two hollow cylinders made from different materials: graphite and aluminum. Figure 5 displays the spatially resolved composition of the cylinders as the fiber is moved relative to them. 10 positions were measured with a 400 µm step resolution in this experiment (Figure S8). The peak area of the main lines of graphite (C_2 band ($\Delta v = 0$) at 516.5 nm) and aluminum (Al (I) at 396.15 nm) were analyzed. By calculating the derivative of the area versus the position, it was determined that the spatial resolution of the system was 670 µm, which is suitable for most catalytic applications where gradients occur at the millimeter to centimeter scale. The time resolution is determined by the repetition rate of the laser, in this work, 10 Hz, meaning that the method is capable of measuring ten elemental spectra per second.

2.5. Propane Dehydrogenation (PDH)

As a second case study, we examined the catalytic propane dehydrogenation (PDH) over a single cylindrical pellet of a VO_X/γ-Al_2O_3 supported catalyst. This reaction system offers several advantages from the method development perspective (Equation (3)). First, it is a stable catalytic system, allowing for reproducible periodic operation between deactivation and

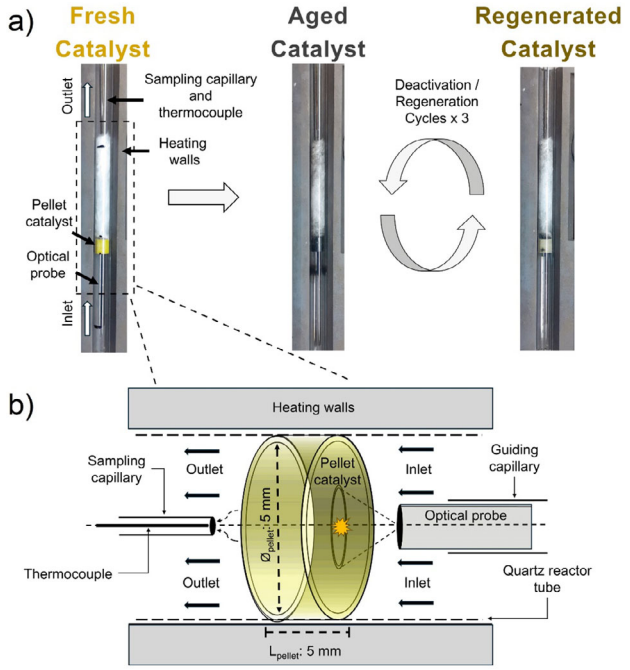

Figure 6. a) Investigation of propane dehydrogenation over a 5x5 mm catalyst pellet by combining time-resolved reactor measurements with in situ LIBS. b) Working principle of elemental spectroscopic, species concentration, and temperature measurements in a fixed-bed reactor.

regeneration cycles. Second, vanadium oxides exhibit distinct visual characteristics that help identify the catalyst's state, particularly whether it is regenerated or deactivated. This provides a valuable source of information to validate the trends observed in LIBS analysis. Lastly, the periodic operation of this system has been extensively researched.[42]

$$C_3H_8 \rightarrow C_3H_6 + H_2 \quad H^0_{298K} = 124KJ/mol \tag{3}$$

Propylene (C_3H_6) has been identified as the main coke precursor during propane dehydrogenation. For this reason, propylene was fed directly as reactant in these experiments.[42] Although propylene dehydrogenation is of limited practical use, this side reaction (Equation (4)) provides a valuable test system for method development, due to its quick and reversible coke formation, allowing to concentrate on method assessment and reproducibility.

$$C_3H_6 \rightarrow \text{coke } (C_XH_Y) + H_2 \tag{4}$$

In this last stage, the capability of the in situ LIBS methodology to detect changes in elemental composition under reaction conditions was evaluated. Three deactivation and regeneration cycles were sequentially performed during which elemental, activity and temperature temporal profiles were simultaneously recorded. The employed methodology is summarized in Figure 6.

Similarly, to the first reaction system, we observed that molecular lines were an excellent diagnostic tool for detection of carbon deposits in the visible region. Therefore, we focused on following the C_2 ($\Delta v = 0$) Swan bands as coking indicator in this set of experiments. Additionally, to avoid potential contributions of propylene in the gas phase to the LIBS carbon signal, the propylene feed was interrupted during each LIBS measurement in the deactivation stage, and the reactor was purged with argon. No feed changes were performed during LIBS measurements in the regeneration stage as no propylene was fed.

Changes in the gas phase composition were analyzed by recording the mass-to-charge ratios of various ions, including H_2 (2 amu), C_3H_6 (15–42 amu), CO (28 amu), O_2 (32 amu), Ar (40 amu), and CO_2 (44 amu). Here, argon was employed as an internal standard. Signal contributions to peak 28 amu were corrected by subtracting the contribution of CO_2.

2.6. Time Resolved Experiments

2.6.1. Deactivation Stage

Figure 7 shows the gas phase composition over time on stream for the first deactivation cycle. As expected, due to increasing catalyst deactivation, the dehydrogenation activity decays exponentially in the first 30 min producing less and less H_2. Simultaneously, the conversion of propylene decreases with time until a plateau is reached at 120 min.

The LIBS profile from Figure 7b complements this information by showing the elemental composition of the catalyst over time. Here, LIBS is indeed capable of detecting carbon deposits under in situ conditions. Deposits are detected starting at 30 min, showing a continuous increase as indicated by the C_2 ($\Delta v = 0$) Swan bands, until a plateau at 60 min is reached. The spectra of the fresh catalyst at the beginning of the process (time 0 min), display molecular bands (AlO at 507,9–514,2 nm) coming from the alumina support.[43,44] Given that the catalyst has a 1,5 wt.% vanadium loading, the presence of the emission lines from the support material is not unexpected. Characteristic lines of vanadium were also detected in their primary emission spectral region covering 430–450 nm (Figure S6). Regarding the temperature profiles, the compact profile reactor exhibited isothermal operation at 675 °C (Figure S7). These findings, along with the results from the subsequent deactivation cycles (Figures S2–S5), are detailed in the Supporting Information.

2.6.2. Regeneration Stage

After the deactivation stage was completed, the reactor was cooled down under inert atmosphere to the regeneration temperature of 500 °C and then purged for 20 min to remove any gaseous hydrocarbons. Inert purging was necessary as the formation of a LIBS plasma can also serve as an ignition source in hydrocarbon-oxygen mixtures.[45,46]

Figure 8 shows the time species profile, indicating how O_2 is consumed during the regeneration process. Under oxidative conditions, carbon deposits are burned off to carbon oxides (CO_x). By integrating the CO_x formation curve, we were able to quantify the amount of carbon deposits over the catalyst, as depicted in Figure 9. As expected from this catalytic system, the regeneration process is quite reversible. The main differ-

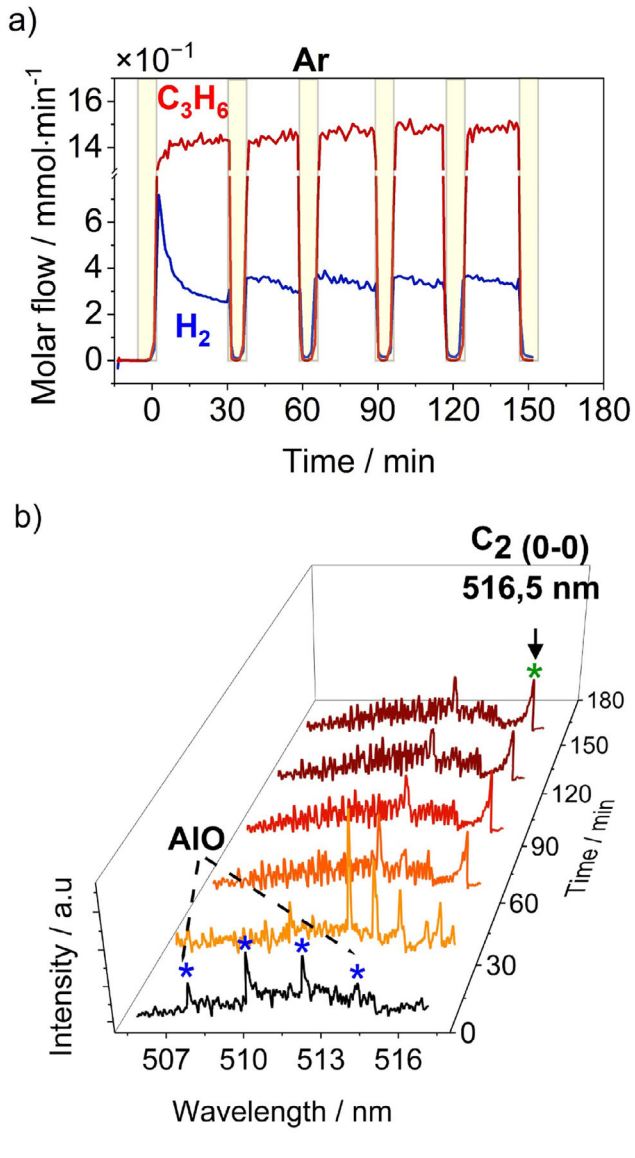

Figure 7. a). Time resolved species profiles for the first deactivation cycle (D_1) using propylene as coke precursor. b) Time resolved LIBS detection of carbonaceous deposits during the deactivation cycle (D_1). Reaction conditions: Feed composition C_3H_6/Ar: 20/80, 80 mL min^{-1}, 675 °C, 1 bar, 5x5 mm catalyst pellet, 1.5 wt.% VO_x/γ-Al_2O_3. LIBS conditions: 1-shoot, 1.8 µs acquisition delay, 55 mJ /pulse, C_2 band ($\Delta v = 0$) at 516,5 nm, and AlO bands in the 512,8–514,8 nm range.

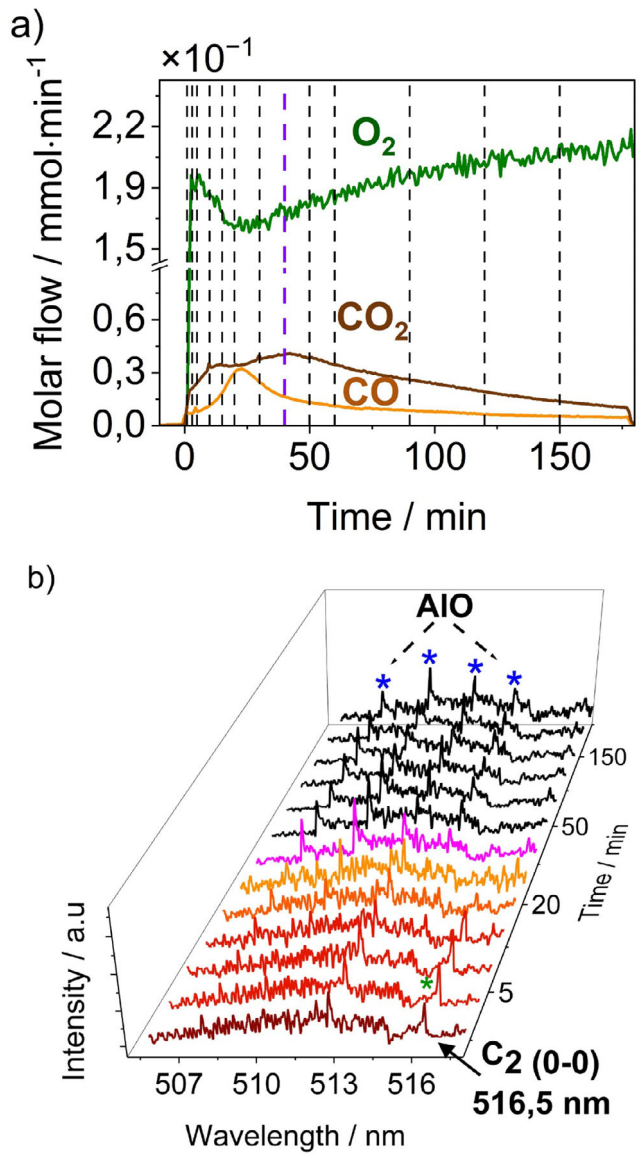

Figure 8. a). Time resolved species profiles for the first regeneration cycle (R_1). b) Time resolved LIBS detection of carbonaceous deposits during regeneration (R_1) Reaction conditions: Feed composition O_2/Ar: 5/95, 80 mL min^{-1}, 500 °C, 1 bar, 5x5 mm catalyst pellet, 1,5 wt.% VO_x/γ-Al_2O_3. LIBS conditions: 1-shoot, 1.8 µs acquisition delay, 55 mJ /pulse, C_2 band ($\Delta v = 0$) at 516,5 nm, and AlO bands in the 512,8–514,8 nm range.

ences between the cycles occur in the first 20 min, with minor variations in carbon content between cycles in the range of 5 wt.%.

In the LIBS profile of Figure 8b, the development of carbon deposits over the catalyst surface is reported. During the first 40 min of regeneration, the C_2 ($\Delta v = 0$) Swan molecular bands continuously diminish, while the AlO molecular lines become stronger and stronger. By comparing the activity data from mass spectrometry (MS) with the elemental composition data from LIBS, a time shift of the point where carbon was fully depleted is observed. The LIBS spectra suggested that the catalyst was regenerated at 40 min, while the MS data indicated that approximately 20% of residual coke deposits remained on the catalyst. This can be explained by taking the sampling configuration (Figure 6b) into account. While the fiber-optic LIBS gives elemental information about the front face of the pellet, the MS sampling capillary sits at the back of the pellet and measures the integral carbon burn-off from the entire pellet. The color changes of the catalyst pellet supported this hypothesis. Vanadium oxide catalysts can change their color in response to the reaction conditions. Deactivated catalysts are dark grey, while fresh and regenerated pellets appear yellow. By employing this visual characteristic and the optical access of the reactor, it was observed that the regeneration process does indeed not occur uniformly at the pellet level.

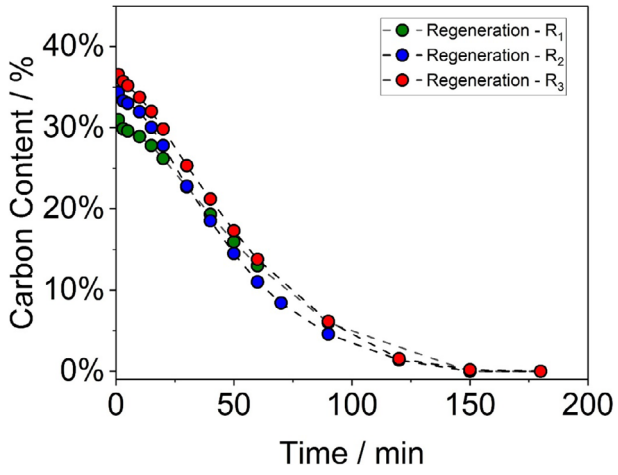

Figure 9. VO_X/γ-Al_2O_3 regeneration profiles for cycles R_1, R_2, and R_3. Reaction conditions: Feed composition O_2/Ar: 5/95, 80 mL min^{-1}, 500 °C, 1 bar, 5x5 mm catalyst pellet, 1,5 wt.% VO_X/γ-Al_2O_3.

By the end of the campaign, no holes or cracks were observed on the frontal pellet face. The use of a large core optical fiber helped reducing the invasiveness of the method compared to the ex situ case. Considering a worst-case scenario with an average ablation rate (AAR) 10 times higher than the rate reported in literature,[31] the initial mass of the pellet and an average carbon content of 30 mg over the cycles, the LIBS sampling rate is estimated to be in the order of 0,3% per pulse on a carbon basis. With an increased spot size in the analysis zone, the laser will sample a broader area with lower penetration and higher surface sensitivity. However, as a tradeoff, the spatial resolution of LIBS will be compromised.

In conclusion, these results show that the fiber-optic LIBS (FO-LIBS) system could detect simultaneously multiple chemical elements here C, V, and Al (Figure S6), under remote and high-temperature conditions. Three deactivation/regeneration cycles support these results, ensuring data reproducibility. The carbon LIBS regeneration profiles correlate well with the gas phase measurements obtained during oxidation. However, the gradients at the pellet level limit a one-to-one correlation in the final stages of regeneration. Additionally, an increased spot size in the analysis zone provided enhanced surface sensitivity and reduced the invasiveness of the method. However, a second fundamental limitation of the method is recognized, covering the topic of process safety. Since LIBS plasma can serve as an ignition source, its use in potentially flammable or explosive reaction atmospheres is limited. If no flammable reaction mixtures are present, e.g., in reforming, pyrolysis, and dehydrogenation reactions that involve hydrocarbons but no oxygen, LIBS can still be applied.

2.6.3. Chemometrics

So far, the qualitative capabilities of LIBS, highlighting trends in elemental distributions based on two reaction systems have been demonstrated. In the next step the quality of the measurements to derive quantitative statements is assessed.

Before conducting this analysis, it is essential to recognize that each LIBS spectrum provides a rich data set containing multi-element information, with each measurement consisting of approximately 51.000 spectral channels. In multi-element samples overlapping wavelengths add complexity to the data. This complexity further increases as more samples are included, and broader spectral ranges, covering the ultraviolet (UV) and visible (VIS) region, are recorded.

Additionally, heterogeneous catalysts are materials with a complex composition including active metals, promoters, supports, and poisons. This broad chemical matrix will directly affect laser-sample coupling during the LIBS process, which will change the relative abundances of neutral and ionized species in the plasma or lead to a process of self-absorption at high analyte concentrations.[47,48] In addition, by extending the methodology to in situ conditions, the effect of the gas atmosphere and temperature will play a crucial role by introducing atmospheric species that can interact with ablated plasma species. The interplay of these phenomena leads to nonlinearities in the emission process. As a result, the relationship between analyte concentration and plasma intensity is altered, complicating any quantitative assessments. Chemometric techniques, particularly partial least squares (PLS), have been reported as effective strategies to address these challenges.[49,50]

2.6.4. Partial Least Squares (PLS)

Partial least squares (PLS) is a multivariate analytical tool commonly used in chemometrics. It focuses on developing mathematical models to analyze complex chemical data. The core concept of PLS is to decompose both the spectral matrix (*X*) (Equation (5)) and the concentration matrix (*Y*) (Equation (6)) into their underlying latent structures. PLS identifies the directions in the X-space that explain the maximum variation in the Y-space by expressing *X* and *Y* in specific forms:

$$X = T * P' + E \tag{5}$$

$$Y = U * C' + G \tag{6}$$

In this context, *T* and *P* represent the scores and loadings of the spectral matrix (*X*), while *U* and *C* denote the scores and loadings of the concentration matrix (*Y*). Two mathematical routines are typically employed to calculate these latent variables: the NIPALS and SIMPLS algorithms. A detailed discussion of these algorithms is beyond the scope of this work; therefore, readers are referred to the existing literature for more comprehensive descriptions.[51,52]

$$U = T * B_{Inner} \tag{7}$$

$$T = W * X \tag{8}$$

In the following intermediate step, regression analysis is performed using the *T* and *U* matrices, as indicated by equation (Equation (7)), the so called "inner relation". Finally, a multiple regression model is obtained by rewriting Equations (6–8) in the

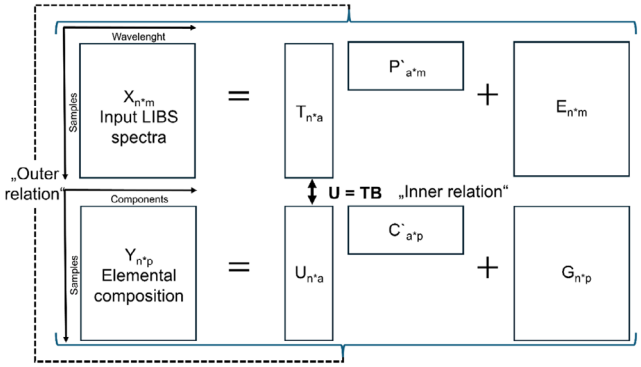

Figure 10. Graphical representation of the partial least squares (PLS) concept.

form:

$$Y = X * (W * B_{Inner} * C') + G \quad (9)$$

$$Y = X * B + Error \quad (10)$$

$$B = W * B_{Inner} * C' \quad (11)$$

The overall decomposition process is depicted schematically in Figure 10. Here, the (*X*) matrix contains channel intensities for each calibration sample, as independent variables, while the (*Y*) matrix holds the elemental concentrations as the dependent variables.

This section develops a PLS model that correlates the carbon content (*Y*) determined in the regeneration phase with the LIBS elemental profiles (*X*). The calibration set, represented by the label "Measured", included the two first regeneration cycles (R_1 and R_2), while the testing set was performed with the last regeneration cycle (R_3). Model construction was performed by using a "leave-one-out" full cross-validation method. This approach involves removing one sample from the calibration set, recalculating the regression model with the remaining samples, and then predicting the composition of the excluded sample, exemplified by "CV validated". Finally, the model, including the entire calibration set, is employed and is represented by the label "Predicted". A region of interest (ROI) covering the spectral window of 388 to 517 nm was chosen for analysis since this zone contains multiple emission lines of vanadium, aluminum, and carbon. Finally, the applicability of the model is tested under extrapolated conditions by predicting coking profiles in subsequent deactivation experiments (D_1, D_2, and D_3). Additional computational details are provided in the experimental section.

Figure 11 displays the carbon parity plot resulting from the regression analysis. Overall, the model effectively captures the data pattern with an average error of 10% (RMSECV = 0029). In the lower carbon content region, some sample outliers are observed. By plotting the data as a time profile, as indicated by Figure 11b,c it becomes apparent that the outliers correspond to the last samples of the regeneration stage for both cycles. The PLS methodology additionally provides insights into the data structure. During the regeneration phases, it identifies outlier samples, which could be due to incorrect measurements or could have chemical significance. In this case, the second reason applies, the outlier samples are a result of non-representative sampling discussed in the previous section.

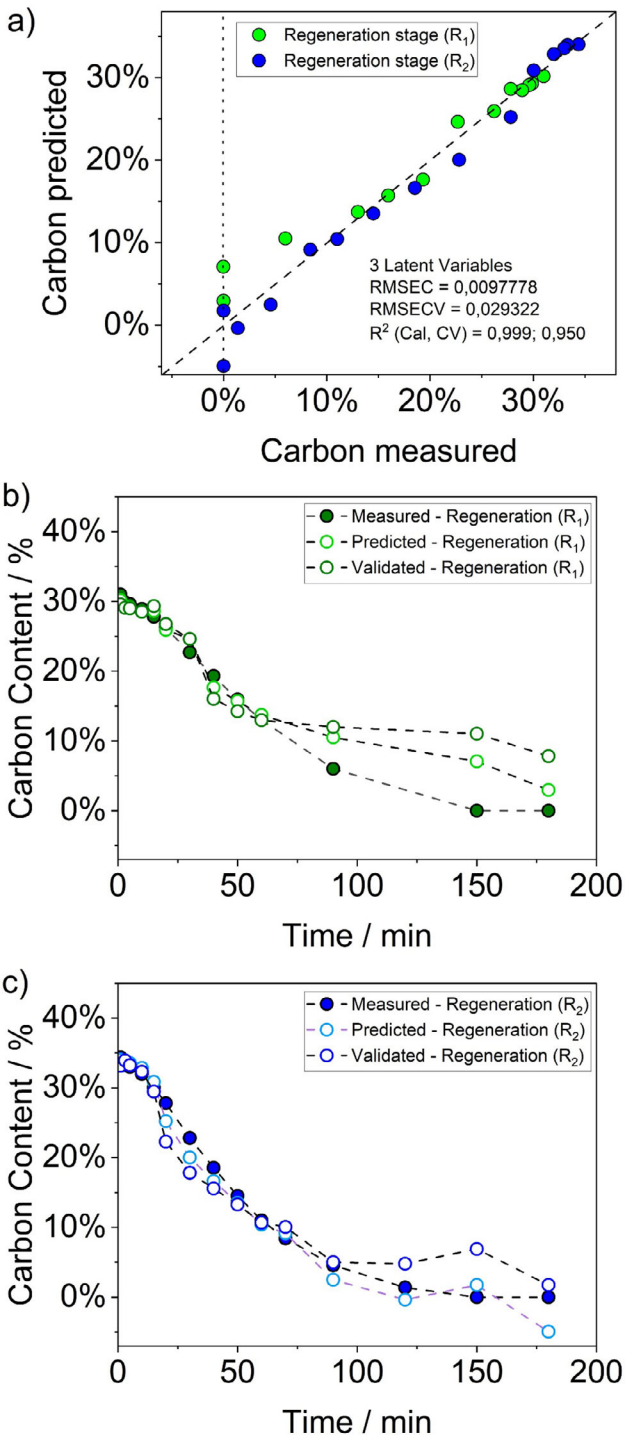

Figure 11. a)Parity plot of PLS model for quantitative assessment of regeneration profiles based on LIBS data (Calibration set: R_1 and R_2). b), c) Measured, predicted and cross-validated regeneration profiles (Calibration set: R_1, and R_2).

In addition, Figure 11a allows the determination of the limit of quantification (LOQ) for the LIBS method. The LOQ can be defined with the "10 σ/S rule".[53,54] Under these conditions, the

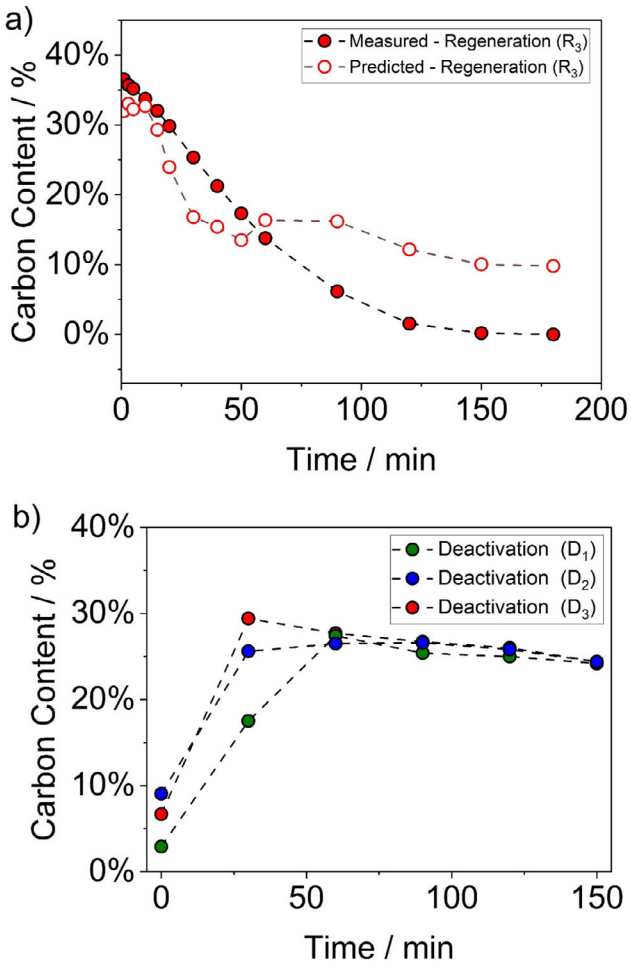

Figure 12. PLS model evaluation by a) prediction of the regeneration cycle (R_3), and b) prediction of deactivation cycles (D_1, D_2, and D_3).

LOQ of carbon is estimated to be 4 wt.%. However, it's important to note that this value is biased due to the outliers at the end of the regeneration cycle. It's also worth mentioning that sensitivity varies depending on the element; for instance, in the case of vanadium, which is present at 1,5 wt. %, emission lines were observed in all measurements. Similarly, impurities of the support material, such as traces of alkali metals (Ca, Na), were commonly observed during the campaign.

In the next step, the model prediction capability was tested with two new data sets, one for the last regeneration cycle (R_3) and the others including all deactivation cycles (D_1, D_2, and D_3). For the first data set (R_3), the model predicts reasonable coking profiles during the first hour of regeneration as indicated by Figure 12. The trends align well with those from other regeneration cycles (R_1 and R_2), and as expected the model deviates in the last section of the regeneration due to non-representative pellet sampling. It is also important to highlight that the model was tested under oxidative conditions and temperatures similar to those in the calibration set.

In the second validation set, the model was evaluated under very different reaction conditions; specifically, it was employed to predict the coking profiles during the deactivation stages (D_1, D_2, and D_3). Overall, the tendency of the deactivation profiles is correctly predicted, as shown in Figure 12b. An increase in coke deposition in the first hour, followed by a plateau until the end of the cycle is observed. However, the total carbon content is underestimated, with deviations of 5 to 10 wt. %, compared to the regeneration cycles.

The primary difference between the data sets was a 145 °C variation in gas temperature and the absence of oxygen. This likely introduces new matrix effects that were not included in the training set (R_1 and R_2). This factor is critical, particularly in spatially resolved systems, with strong gradients in atmospheric and temperature conditions along the reactor. Such variations make it challenging to derive quantitative descriptions of the elemental composition of the catalysts along the catalytic bed.

Summarizing, multivariate analysis, or more specifically PLS, has been found to be a good alternative for exploiting the vast amount of information that a LIBS spectrum provides. Additionally, in combination with preprocessing techniques, it allows for compensation of matrix effects. From a mathematical perspective, the PLS model shows acceptable regression statistics. Sensitivity is observed to be element specific with a quantification limit for carbon in the range of 6 to 12 wt.%. The calibration strategy followed in this section limits the use of the model to the regeneration phase. Extrapolation to deactivation conditions introduce larger error bars, but tendencies are still correctly predicted.

3. Conclusion

The present work explores the application of LIBS as diagnostic tool for catalytic fixed-bed reactors. Following a systematic approach covering ex situ catalyst characterization, remote setup development, and in situ characterization, distributions of active metal and poisons (Ni, V, and C) were measured in combination with activity performance and temperature profiles. The dry reforming of methane (DRM) on supported Ni/γ-Al_2O_3 and the propane dehydrogenation (PDH) on supported VO_x/γ-Al_2O_3 were chosen as test systems.

Species, temperature and LIBS profiles during dry reforming of methane, even though measured ex situ, provided a proof of concept by delivering spatially resolved correlations between activity performance, temperature, and catalyst elemental distribution along the reactor bed. Carbon deposition is already present in the inlet-middle region of the reactor, while near outlet positions are characterized by a less severe carbon fingerprint. The higher water and hydrogen content in this region in combination with an increased temperature seems to facilitate coke gasification. Scanning electron microscope images and energy dispersive spectroscopy confirm the observed trends in the elemental distribution of carbon and nickel.

In the second case study, the applicability of LIBS as in situ diagnostic technique was demonstrated for the first time. In these experiments, the periodic operation performance of supported VO_x/γ-Al_2O_3 catalyst pellets during propylene dehydrogenation was investigated. Multielement information of carbon and vanadium was obtained and complemented by simultaneous species and temperature time profiles. Overall, the carbon

LIBS profiles correlate well with the gas phase measurements obtained during periodic operation. In the deactivation stage, activity and elemental information were correlated by monitoring the gas phase composition and carbon molecular emission lines. During this stage, hydrogen production decreases exponentially while carbon deposits increase with time-on-stream. In the regeneration stage, coke deposits are burned-off under oxidative conditions as CO and CO_2, leading to a decreasing coke loading. The application of chemometric methods, in particular, partial least squares regression provided a good alternative to make quantitative statements about catalyst elemental composition and to exploit the vast amount of information provided by LIBS. The proposed PLS model allows to make quantitative statements about the regeneration state of the catalyst. However, when the model was applied to deactivation conditions, the carbon content was underestimated, even though the qualitative coking behavior was correctly predicted. One of the major causes of this different model performance is most likely the strong effect of gas phase atmosphere on LIBS plasma formation and decay.

It is important to realize that in the context of "carbon analysis", LIBS, while providing both qualitative and quantitative information about the concentration of carbon and other elements in the ablated volume, it does not provide any information on how these elements are chemically bound, viz., in which chemical form they make up the sample. In contrast, techniques such as Raman spectroscopy provide information on the chemical state of the elements, in the case of carbon, for example, whether the carbon is graphitic, disordered, sp2-hybridized, sp3-hybridized, etc., information that can help to understand the deactivation mechanism. Recent studies have even reported localized carbonaceous characterization at the nanoscale level.[9,55] As Raman-spectroscopy is hardly quantifiable, LIBS and Raman provide complementary information. Given that both techniques employ lasers, the integration of Raman and LIBS systems could enhance our understanding by combining both methods.

From the methodological point of view, a simple and cost-effective fiber-optic LIBS setup (FO-LIBS) that allows for the examination of hard-to-reach areas, such as inside catalytic reactors, was developed. The setup can perform front and side sampling with spatial and time resolutions in the range of 700 µm and seconds, respectively, which is sufficient for most catalytic applications.

Overall, it was demonstrated that LIBS meets most of the requirements for an in situ analysis technique. However, its partially destructive behavior and the effect of gas atmosphere are recognized as the most critical parameters limiting the universal application on fixed-bed reactors. It would be beneficial to have a fresh position for each sample point, that allows for signal accumulation improving sampling statistics. It is anticipated that the potential of LIBS lies in a different type of reactor configuration, such as a fluidized bed reactors where the catalyst is in continuous motion, providing fresh sample particles for each laser shot. A second potential application involves using LIBS in liquid phase and multiphase reactors, where the sample in the laser focus is constantly renewed. Additionally, sampling the liquid phase will provide the additional advantage of sample homogeneity at a molecular level.

Application of LIBS is not limited to the chemical systems studied in the presented work. Alternative systems could include fossil fuel replacement technologies, such as methanol-to-hydrocarbons, or biomass and plastic waste pyrolysis.[56] The main limitation resides in the reaction atmosphere of the systems, where fuel/air mixtures must be avoided. In these cases, LIBS could be applied, for example, to quantify carbonaceous species, either during the reaction or in the regeneration phase,[57] or alternatively, as a process diagnosis tool for evaluating elemental impurities such as CHONS, halogens, and metals in pyrolysis oils.[29,58,59] Table 1 provides a summary of the main advantages and disadvantages of the method from our perspective, along with potential strategies to address its current limitations.

4. Experimental Section

4.1. Methane Dry Reforming (DRM)

The methodology employed in the first case study involved two types of measurements. First, spatially resolved species and temperature measurements were performed in a semi-pilot profile reactor. Second, ex situ LIBS characterization of samples extracted layer by layer from the catalyst bed was performed, complemented by scanning electron microscopy measurements on selected catalyst spheres (Figure 1).

4.2. Activity Measurements–Spatial Species Profiles

Activity measurements were performed on 20 wt.% supported Ni/γ-Al_2O_3 spheres of 1 mm diameter. The catalyst was prepared by incipient wetness impregnation. The catalyst preparation followed the procedure reported elsewhere.[60–62]

Overall, the experimental setup consisted of three main parts: i) a gas dosing system, ii) a semi-pilot spatial profile reactor, and iii) gas analytics. The working principle of the semi-pilot profile reactor is described in detail in a previous publication.[63] Shortly summarized, the profile reactor consists of a quartz reactor tube (OD 38 mm, ID 18 mm) surrounded by a split furnace connected to a power supply and temperature controller to heat the catalyst. High-resolution gas species profiles are measured with a stainless-steel capillary (OD 700 µm, ID 520 µm) that runs through the center of the quartz tube and the catalyst bed. The sampling capillary has four small side sampling orifices (4 x 50 µm), all at the same height of the capillary and is connected to a stainless-steel holder mounted to a rotary and linear stage, allowing for precise movement and rotation. To the outside, the capillary is sealed with a thin layer of grease to allow smooth movement and prevent gas bypassing. Gas species sampling is achieved by mass spectrometry (MS, Balzers). Inside the sampling capillary, a type-K thermocouple (OD 250 µm) (TMH GmbH), tip-aligned with the orifice, is used to measure the gas temperature at the sampling position. By moving the sampling, capillary with the thermocouple inside up and down, spatially resolved species and temperature profiles can be recorded.

Catalyst activity profiles were measured using a catalyst bed of 30 mm in length, packed with 1 mm diameter spheres. A total flow rate of 500 mL min^{-1} (at standard temperature and pressure) was employed, corresponding to a gas hourly space velocity (GHSV) of 5890 h^{-1}. The reaction mixture consisted of methane (CH_4), carbon

Table 1. Overview of the figures of merit for fiber-based LIBS in heterogeneous catalysis research.

Figure of merit	Achievements-present work	Limitations
Compatibility	Structure-activity elemental correlations (e.g., LIBS-MS)	• Bulk-average characterization (mm-scale), no multi-scale structure-activity correlations (nm-scale)
Multielement	Ni, C and V elemental distributions	• Element specific detection limit, elements in small (ppm) concentrations might not be detected (surface adsorbates, promoters)
Quantification	Multivariate model development for carbonaceous deposits quantification (PLS-1)	• Element specific detection limit; plasma self-absorption at higher concentrations[64,48]
Remote	Fiber optic pulse delivery and signal collection	• Melt temperature, damage threshold and signal attenuation from optical fibers
Resolution	• 1D-Spatial resolution: 700 µm • Temporal resolution: 10 Hz	• 1D-Spatial resolution: Fiber dimensions and step-motor precision • 2D/3D-Elemental maps not accessible • Time resolution: Laser repetition rate
Figure of merit	Disadvantages	Suggestions
Semi destructive	Surface invasiveness and crater formation	• Single shot sampling • Fresh position–reactor type (e.g., FBR) • Liquid media analysis–multiphase reactors (e.g., BCR) • Reactor scale (laboratory vs industrial) • Process diagnostics tool, not operando research
Atmosphere	Changes in plasma chemistry, matrix effects, and signal overlap	• Multivariate chemometric analysis
Operational safety	• Ignition source on HC´s/oxidant mixtures • Class-4 laser safety	• Inert flush system • Laser protective equipment (e.g., safety glasses, windows)

dioxide (CO_2), and argon (Ar) as an internal standard, with a molar composition of 25/25/50 respectively. The split furnace surrounding the quartz reactor tube was heated to 720 °C and the reaction was performed under atmospheric pressure. Before starting the profile measurements, the reactor was heated at a rate of 10 °C per minute under inert conditions. Following this, the gas feed was switched to the reaction feed and the system was allowed to stabilize for 90 min until a steady state was reached. Spatially resolved measurements were then conducted with a scan rate of 440 µm per second. Two profile replicates were measured during these experiments.

4.3. Ex Situ LIBS

After the species profile measurements, the spent catalyst from different reactor zones was extracted and investigated by ex situ LIBS. In total, 53 cross sections were evaluated. To ensure a representative sampling three LIBS measurements at different radial positions were recorded, giving a total of 159 spectra.

For this purpose, a commercial LIBS setup (LIBSpector, LTB Berlin) was employed. The optical setup consists of a sample housing with a motorized XYZ stage for probe scanning. Additionally, online video monitoring allows precise control over the sampling position. Plasma ignition is achieved by a built-in Q-switched Nd:YAG laser (Nano, Litron) working at 1064 nm wavelength, pulse length of 4–7 ns, repetition rate of 20 Hz, and maximum pulse energy of 130 mJ. A double echelle spectrograph (Aryelle Butterfly, LTB Lasertechnik Berlin) equipped with an EMCCD detector (Newton, Andor) provides precise elemental analysis. The spectrograph is equipped with two separate spectral ranges, 192–330 nm (UV) and 310–930 nm (VIS) that can be alternatively switched with each other.

In this configuration, the Nd:YAG laser is directly focused on the sample by a lens system. Since LIBS formation is a transient process, laser, camera, and detector must be synchronized. This is achieved by a trigger unit (LIBS Control, LTB Lasertechnik Berlin), allowing the acquisition of the LIBS signal at any desired plasma lifetime. Finally, the signal is collected by a lens/mirror optical system and coupled into a solarization-resistant optical fiber (0.22 NA, 400 µm

core, LTB Lasertechnik Berlin) that transmits the light to the spectrometer for dispersion and analysis. A single-shot LIBS analysis was performed on the aged catalyst with the following parameters. Pulse energy, 50 mJ, spot size of ~ 600 µm, and plasma lifetime of 1.8 µs. Data evaluation was assisted by employing the NIST database in combination with PLASUS SpecLine software (PLASUS GmbH). Spectrometer wavelength calibration was ensured by constantly checking the calibration status of the device during experiments with the help of a built-in Hg lamp.

4.4. Propane Dehydrogenation (PDH)

The methodology employed in this second case study included the simultaneous measurement of activity information and in situ LIBS analysis in a temporal-resolved manner (Figure 6). In the last part, the results were complemented by chemometrics analysis.

4.5. Activity Measurements – Time Species Profiles

Activity measurements were performed with a 1.5 wt. % supported VO_X/γ-Al_2O_3 single cylindrical pellet catalyst (length x width: 5 x 5 mm). The catalyst was prepared by wetness impregnation. The detailed catalyst preparation procedure can be found elsewhere.[65]

Overall, the setup consists of four main parts: i) LIBS optical setup, ii) a compact profile reactor, iii) a gas dosing system, and iv) gas analytics. The working principle of the compact profile reactor (CPR, Reacnostics GmbH) closely resembles that of the semi-pilot profile reactor used in the first case study. However, the major difference between the two reactors is that in the CPR, the sampling capillary is fixed, and the catalyst bed is translated along the sampling orifice (Figure 6), while in the semi-pilot profile reactor used for methane dry reforming, the catalyst bed was fixed and the capillary was translated. A more detailed description of the reactor can be found in previous publications.[10,66] In brief, the CPR consists of a fused silica reactor tube (OD 6 mm, ID 5 mm), filled with a catalyst bed up to 6 cm in length kept in place with quartz wool plugs. Gases are introduced via mass flow controllers (MFC's) and preheated in a 4 cm preheating zone to the desired temperature before entering the catalyst bed. A stainless-steel sampling capillary (OD 700 µm, ID 520 µm) runs through the center of the catalyst bed, equipped with side-sampling orifices (4 x 50 µm), all at the same height of the capillary. Multiple orifices are used to reduce the risk of plugging. Gas species sampling is achieved by mass spectrometry (MS, Hiden HPR 20). Inside the capillary, a type-K thermocouple (OD 250 µm, TMH GmbH) tip-aligned with the orifices measures the gas phase temperature.

Catalyst activity profiles were measured with a total flow rate of 80 mL min^{-1} (at standard temperature and pressure) resulting in a gas hourly space velocity (GHSV) of 48900 h^{-1}. In this series of experiments, three deactivation-regeneration cycles were conducted. Each cycle consisted of a 2.5 h deactivation stage followed by a 3.0 h regeneration stage.

During the deactivation phase, the reaction mixture consisted of propylene (C_3H_6) and argon (Ar) as an internal standard, with a molar composition of 20/80, respectively. The reaction was carried out at a temperature of 675 °C under atmospheric pressure. Before initiating the profile measurements, the reactor was heated at a rate of 20 °C per minute under inert conditions. Following this, the gas feed was switched to deactivation conditions, and gas phase deactivation profiles were measured using a mass spectrometer. Simultaneously, LIBS measurements were performed every 30 min under an argon atmosphere. Once the deactivation phase was finished, the reactor was cooled down to 500 °C under inert conditions. Once the target temperature was reached, the reactor was purged for an additional 20 min to eliminate any residual hydrocarbons. Following this, the regeneration process began using a lean mixture of oxygen (O_2) and argon (Ar) in a molar ratio of 5/95, with a flow rate of 80 mL min^{-1}. During the initial minutes of regeneration (at 1, 3, 5, and 10 min), a higher LIBS sampling frequency was employed to capture the initial rate of carbon removal.

4.6. Intra-Reactor Profile LIBS

In contrast to ex situ LIBS, where the catalyst spheres extracted from the profile reactor after reaction were analyzed by direct laser shots in the commercial LIBSpector, in situ LIBS offers the advantage of remote analysis by coupling the laser pulse into an optical fiber. This allows access to difficult areas, for example, the interior of chemical reactors, extending the application range of LIBS significantly. Spectroscopic data were collected by introducing an optical fiber into the CPR (Figure 6b). By keeping the fiber in a fixed position, repetitive laser shots can be used to record temporal changes in the elemental composition of the catalyst. Spatially resolved profiles could be obtained by using a side-fire fiber and laterally shifting the fiber with micrometer precision along the probe volume (Figure 5). This technique will eventually enable measuring composition profiles of catalysts in fixed-bed reactors and, if combined with species- and temperature profiling, also *operando* elemental profiles. In the present work, the optical fiber was inserted through a stainless-steel guiding capillary to hold the fiber at the center of the reactor tube and additionally protect the distal fiber end from damage during the assembly process. The working principle of the method is illustrated in Figure 13.

The optical setup consisted of a Q-switched Nd:YAG laser (Brilliant, Quantel) working at 1064 nm wavelength, a pulse length of 4–7 ns, a repetition rate of 10 Hz, and a maximum pulse energy of 360 mJ. Laser-fiber coupling was achieved by first adjusting the coupling energy to a level of 100 mJ / pulse by adjusting the Q-switch delay of the laser. Beam homogenizing was performed with the help of a Micro Lens Array (MLA, Süss MicroOptics 18–00183). The beam was then focused with a high-power N-BK7 plano convex lens of 75 mm focal length (Thorlabs LA1608-YAG) into a multimode fused-silica fiber (Thorlabs FT1500 UMT), of 0.5 m length, a core diameter of 1500 µm, and a numerical aperture of 0.39 NA. Precise fiber alignment was assisted by an XYZ-Axis stage (Thorlabs MB616D/M), ensuring that around 85 % of the fiber inlet face was covered during injection.

Decoupling of the LIBS signal was achieved by a 90° off-axis parabolic mirror (Thorlabs MPD229H-F01). The parabolic mirror has a hole in the center allowing the excitation laser beam to pass through for coupling into the optical fiber. The LIBS signal returning through and emitting from the same fiber is collimated by this mirror and reflected into a UV-grade plano-convex lens of 30 mm focal length (EKSMA optics 110–1203E) which focuses the LIBS signal into a solarization-resistant multimode fiber (0.22 NA, 400 µm core, LTB Lasertechnik Berlin) which finally guides the light into a spectrograph (Aryelle Butterfly, LTB Lasertechnik Berlin) for dispersion and detection. A delay generator (LIBS control, LTB Lasertechnik Berlin) was used to synchronize the laser triggering with the camera detector. Similar to the ex situ experiments, wavelength calibration was ensured by consistently performing calibrations during the measurements. Data evaluation was facilitated by utilizing the NIST database and Plasus software.

4.7. Chemometrics

Multivariate analysis was conducted using the PLS_Toolbox from MATLAB (Eigenvector Research, Inc.). The partial least squares (PLS)

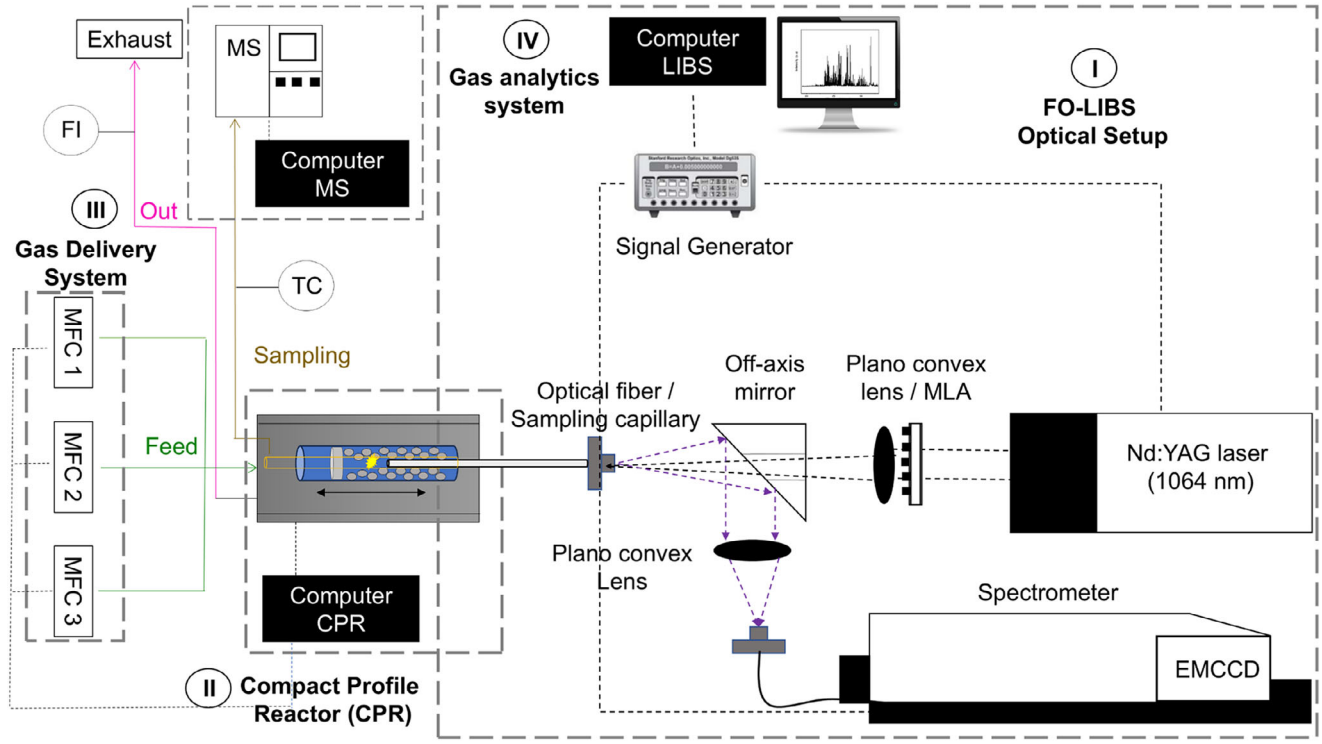

Figure 13. Schematic representation of the experimental setup employed on in situ LIBS measurements. (I) Remote LIBS setup; (II) Compact profile reactor (CPR); (III) Gas delivery system (MFCs); (IV); Gas analytics system (MS).

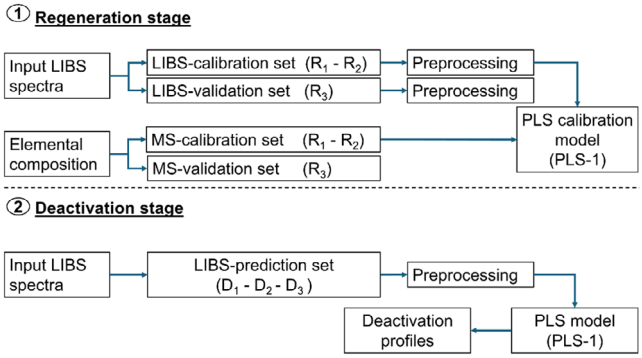

Figure 14. Overview of the methodology followed for PLS model construction by combination of MS-LIBS time profiles.

routine involves creating a regression model that establishes a correlation between two matrices: the LIBS spectra (*X*) and the elemental concentrations (*Y*). In this study, the total amount of carbon deposits was calculated by integrating the CO and CO_2 evolution profiles during carbon burn-off from the VO_X/γ-Al_2O_3 single pellets after propylene dehydrogenation. The carbon content is reported as an atomic fraction, considering the presence of vanadium (V), aluminum (Al), and oxygen (O) in the catalyst matrix. Before model construction, data pretreatment including total area normalization and baseline offset removal was performed. A region of interest (ROI) covering the spectral range from 388 to 517 nm was selected for the PLS model development.

The multivariate analysis was conducted in two stages: model construction and model validation. For model construction, the calibration set included 28 spectra from regeneration cycles R_1 and R_2. To validate the regression model, a "leave-one-out" full cross-validation method was used. This method involves removing one sample from the training set, recalculating the regression model with the remaining samples, and then predicting the composition of the excluded sample. For model validation, the prediction set comprised 14 spectra from regeneration cycle R_3. The validity of the model was further tested under extrapolated deactivation conditions. In this case, the prediction set included all 18 spectra measured across three deactivation cycles: D_1, D_2, and D_3. The overall strategy is summarized in Figure 14.

Acknowledgments

The authors thank Michael Schmidt (Reacnostics GmbH) and Dominik Schiller (LTB Berlin) for technical support through this project. The authors also thank Prof. Dr. Christof Hamel for the guidance and fruitful discussion on the topic of propane dehydrogenation. The authors are grateful to Klaus Mandel and Patrick Kißling for their assistance with SEM-EDS catalyst characterization.

Open access funding enabled and organized by Projekt DEAL.

Conflict of Interests

The authors declare no conflict of interest.

Data Availability Statement

The data that support the findings of this study are available from the corresponding author upon reasonable request.

Keywords: Catalyst deactivation · Chemometrics · Heterogeneous catalysis · In situ LIBS · Laser spectroscopy · Profile reactor

[1] K. A. Christensen, *Comput. Aided Chem. Eng.* **2007**, *23*, 311.
[2] A. Urakawa, A. Baiker, *Top. Catal.* **2009**, *52*, 1312-1322.
[3] F. Zaera, *J. Catal.* **2021**, *404*, 900-910.
[4] K. Morgan, J. Touitou, J. Choi, C. Coney, C. Hardacre, J. Pihl, C. Stere, M. Kim, C. Stewart, A. Goguet, W. Partridge, *ACS Catal.* **2016**, *6*, 1356-1381.
[5] L. Lukashuk, K. Foettinger, *Johnson Matthey Technol. Rev.* **2018**, *62*, 316.
[6] J. D. Winefordner, I. B. Gornushkin, T. Correll, E. Gibb, B. W. Smith, N. Omenetto, *J. Anal. At. Spectrom.* **2004**, *19*, 1061.
[7] M. K. Tiwari, In: *X-Ray Fluorescence in Biological Sciences*, Wiley, New Jersey, **2022**, pp. 115–149.
[8] F. Meirer, B. M. Weckhuysen, *Nat. Rev. Mater.* **2018**, *3*, 324-340.
[9] S. Das, R. Pashminehazar, S. Sharma, S. Weber, T. L. Sheppard, *Chem. Ing. Tech.* **2022**, *94*, 1591.
[10] B. Wollak, D. E. Doronkin, D. Espinoza, T. Sheppard, O. Korup, M. Schmidt, S. Alizadehfanaloo, F. Rosowski, C. Schroer, J.-D. Grunwaldt, R. Horn, *J. Catal.* **2022**, *408*, 372-387.
[11] D. W. Hahn, N. Omenetto, *Appl. Spectrosc.* **2012**, *66*, 347-419.
[12] J. Laserna, J. M. Vadillo, P. Purohit, *Appl. Spectrosc.* **2018**, *72*, 35–50.
[13] D. A. Cremers, R. C. Chinni, *Appl. Spectrosc. Rev.* **2009**, *44*, 457–506.
[14] S. M. Clegg, R. B. Anderson, N. Melikechi, *Laser-Induced Breakdown Spectroscopy: Theory and Laboratory Spectra of Geologic Materials*, Cambridge University Press, Cambridge, **2019**.
[15] J. El Haddad, L. Canioni, B. Bousquet, *Spectrochim. Acta B At. Spectrosc.* **2014**, *101*, 171–182.
[16] P. Lucena, L. M. Cabalín, E. Pardo, F. Martín, L. J. Alemany, J. J. Laserna, *Talanta* **1998**, *47*, 143–151.
[17] P. Lucena, J. M. Vadillo, J. J. Laserna, *Appl. Spectrosc.* **2001**, *55*, 267–272.
[18] P. Lucena, J. M. Vadillo, J. J. Laserna, *J. Anal. At. Spectrom.* **2002**, *17*, 548–551.
[19] F. Trichard, L. Sorbier, S. Moncayo, Y. Blouët, C.-P. Lienemann, V. Motto-Ros, *Spectrochim. Acta B At. Spectrosc.* **2017**, *133*, 45–51.
[20] F. Trichard, F. Gaulier, J. Barbier, D. Espinat, B. Guichard, C.-P. Lienemann, L. Sorbier, P. Levitz, V. Motto-Ros, *J. Catal.* **2018**, *363*, 183–190.
[21] G. D. Wehinger, M. Kraume, V. Berg, O. Korup, K. Mette, R. Schlögl, M. Behrens, R. Horn, *AIChE J.* **2016**, *62*, 4436–4452.
[22] K. Wittich, M. Krämer, N. Bottke, S. A. Schunk, *ChemCatChem* **2020**, *12*, 2130–2147.
[23] A. Tarasov, H. Düdder, K. Mette, S. Kühl, K. Kähler, R. Schlögl, M. Muhler, M. Behrens, *Chem. Ing. Tech.* **2014**, *86*, 1916–1924.
[24] H. Düdder, K. Kähler, B. Krause, K. Mette, S. Kühl, M. Behrens, V. Scherer, M. Muhler, *Catal. Sci. Technol.* **2014**, *4*, 3317–3328.
[25] T. Ctvrtnickova, M. P. Mateo, A. Yañez, G. Nicolas, *J. Optoelectron. Adv. Mater.* **2010**, *12*, 668–673.
[26] M. Kuzmanovic, D. Rankovic, M. Trtica, J. Ciganovic, J. Petrovic, J. Savovic, *Spectrochim. Acta B At. Spectrosc.* **2019**, *157*, 37–46.
[27] Q. Zhang, Y. Liu, W. Yin, Y. Yan, Q. Tang, G. Xing, *J. Anal. At. Spectrom.* **2020**, *35*, 341–346.
[28] D. Wang, P. Littlewood, T. J. Marks, P. C. Stair, E. Weitz, *ACS Catal.* **2022**, *12*, 8352–8362.
[29] E. T. C. Vogt, D. Fu, B. M. Weckhuysen, *Angew. Chem., Int. Ed.* **2023**, *62*, e202300319.
[30] R. Colombo, G. Moroni, C. Negri, G. Delen, M. Monai, A. Donazzi, B. M. Weckhuysen, M. Maestri, *Angew. Chem., Int. Ed.* **2024**, *63*, e202408668.
[31] J. M. Vadillo, J. Laserna, *Spectrochim. Acta B At. Spectrosc.* **2004**, *59*, 147-161.
[32] R. Setchell, D. Berry, *Proc. SPIE*, **2007**, *6662*, 203.
[33] R. E. Neuhauser, U. Panne, R. Niessner, *Appl. Spectrosc.* **2000**, *54*, 923–927.
[34] T. Schmidt-Uhlig, P. Karlitschek, M. Yoda, Y. Sano, G. Marowsky, *Eur. Phys. J. AP* **2000**, *9*, 235–238.
[35] A. K. Rai, H. Zhang, F. Y. Yueh, J. P. Singh, A. Weisberg, *Spectrochim. Acta B At. Spectrosc.* **2001**, *56*, 2371–2383.
[36] D. G. Fobar, X. Xiao, M. Burger, S. Le Berre, A. T. Motta, I. Jovanovic, *Prog. Nucl. Energy* **2018**, *109*, 188–194.
[37] D. Beddows, O. Samek, M. Liška, H. Telle, *Spectrochim. Acta B At. Spectrosc.* **2002**, *57*, 1461–1471.
[38] R. Noll in, *Laser-Induced Breakdown Spectroscopy: Fundamentals and Applications*, Springer, Berlin Heidelberg, Berlin, Heidelberg **2012**, pp. 17–46.
[39] G. A. Theriault, S. H. Lieberman, *Proc. SPIE*, **1996**, *2835*, 83.
[40] A. I. Whitehouse, J. Young, I. M. Botheroyd, S. Lawson, C. P. Evans, J. Wright, *Spectrochim. Acta B At. Spectrosc.* **2001**, *56*, 821–830.
[41] H. Abbasi, R. Guzman, P. C. Cattin, A. Zam, *Opt. Lasers Eng.* **2022**, *148*, 106765.
[42] A. Brune, A. Seidel-Morgenstern, C. Hamel, *Catalysts* **2020**, *10*, 1374.
[43] Q. Wang, A. Chen, W. Xu, D. Zhang, Y. Wang, S. Li, Y. Jiang, M. Jin, *Opt. Laser Technol.* **2020**, *122*, 105862.
[44] E. Clavé, D. Vogt, S. Schröder, S. Maurice, B. Bousquet, *Spectrochim. Acta B At. Spectrosc.* **2022**, *194*, 106464.
[45] J. V. Pastor, J. M. García-Oliver, A. García, M. Pinotti, *Energy Convers. Manage.* **2016**, *120*, 144–156.
[46] M. Weinrotter, H. Kopecek, E. Wintner, M. Lackner, F. Winter, *Int. J. Hydrogen Energy* **2005**, *30*, 319–326.
[47] C. Aragón, J. A. Aguilera, *Spectrochim. Acta B At. Spectrosc.* **2008**, *63*, 893–916.
[48] R. Hai, Z. He, X. Yu, L. Sun, D. Wu, H. Ding, *Opt. Express* **2019**, *27*, 2509–2520.
[49] S. M. Clegg, E. Sklute, M. D. Dyar, J. E. Barefield, R. C. Wiens, *Spectrochim. Acta B At. Spectrosc.* **2009**, *64*, 79–88.
[50] J.-B. Sirven, B. Bousquet, L. Canioni, L. Sarger, *Anal. Chem.* **2006**, *78*, 1462–1469.
[51] P. Geladi, B. R. Kowalski, *Anal. Chim. Acta* **1986**, *185*, 1–17.
[52] S. de Jong, *Chemom. Intell. Lab. Syst.* **1993**, *18*, 251–263.
[53] M. Ortiz, L. Sarabia, A. Herrero, M. Sánchez, M. Sanz, M. Rueda, D. Giménez, M. Meléndez, *Chemom. Intell. Lab. Syst.* **2003**, *69*, 21–33.
[54] S. A. Gegenschatz, F. A. Chiappini, C. M. Teglia, *Anal. Chim. Acta* **2022**, *1209*, 339342.
[55] M. Filez, P. Walke, H. Le-The, S. Toyouchi, W. Peeters, P. Tomkins, J. C. T. Eijkel, S. De Feyter, C. Detavernier, D. E. De Vos, H. Uji-I, M. B. J. Roeffaers, *Adv. Mater.* **2024**, *36*, 2305984.
[56] DECHEMA, CATALYSIS - An interdisciplinary key technology for a sustainable economic development **2023** can be found under https://dechema.de/en/Research/Reports+and+position+papers/2010+Roadmap+of+German+Catalysis+Research.html.
[57] V. Paunović, V. Sushkevich, P. Rzepka, L. Artiglia, R. Hauert, S. Sik Lee, J. A. van Bokhoven, *J. Catal.* **2022**, *407*, 54–64.
[58] A. A. Bol'shakov, S. J. Pandey, X. Mao, C. Liu, *Spectrochim. Acta B At. Spectrosc.* **2021**, *179*, 106094.
[59] M. Kusenberg, A. Zayoud, M. Roosen, H. D. Thi, M. S. Abbas-Abadi, A. Eschenbacher, U. Kresovic, S. de Meester, K. M. van Geem, *Fuel Process. Technol.* **2022**, *227*, 107090.
[60] I. Chen, S. Y. Lin, D. W. Shiue, *Ind. Eng. Chem. Res.* **1988**, *27*, 926–929.
[61] I. Chen, D. W. Shiue, *Ind. Eng. Chem. Res.* **1988**, *27*, 429–434.
[62] C. H. Bartholomew, R. J. Farrauto, *J. Catal.* **1976**, *45*, 41–53.
[63] R. Horn, O. Korup, M. Geske, U. Zavyalova, I. Oprea, R. Schlögl, *Rev.sci. instrum.* **2010**, *81*, 64102.
[64] J. D. Pedarnig, S. Trautner, S. Grünberger, N. Giannakaris, S. Eschlböck-Fuchs, J. Hofstadler, *Appl. Sci.* **2021**, *11*, 9274.
[65] B. M. Weckhuysen, D. E. Keller, *Catal. Today* **2003**, *78*, 25–46.
[66] B. Wollak, D. Espinoza, A.-C. Dippel, M. Sturm, F. Vrljic, O. Gutowski, I. G. Nielsen, T. L. Sheppard, O. Korup, R. Horn, *J. Synchrotron Radiat.* **2023**, *30*, 571–581.

Manuscript received: June 12, 2025
Revised manuscript received: August 27, 2025
Accepted manuscript online: September 5, 2025
Version of record online: ■■, ■■